Cho et al. *NPG Asia Materials* (2025) 17:37
https://doi.org/10.1038/s41427-025-00618-3

NPG Asia Materials

ARTICLE Open Access

Impact-resistant, haze-free, 3D-printable transparent block copolymer resin via photopolymerization-induced microphase separation

Suchan Cho[1], Young Soo Lee[1,2], Subi Choi[3], Yunmi Chae[4], Sungmin Park[4], Suk-kyun Ahn[3] and Myungeun Seo[1,5]

Abstract

Incorporating rubbery domains into glassy polymers is an effective route to improve toughness and impact strength. However, retaining the transparency of the composite material over a wide temperature range with enhanced mechanical attributes is challenging because of a mismatch in refractive indices with changing temperatures, limiting their applications as optical materials. Here, we report photopolymerization-induced microphase separation as a strategy for the fabrication of transparent, temperature-resistant nanostructured polymeric materials. Taking poly(methyl methacrylate) (PMMA) as the glassy component for its renowned high transparency, we perform controlled radical polymerization upon light exposure to transform the whole polymerization mixture into a cross-linked block polymer material, where a bicontinuous nanostructure consisting of PMMA and cross-linked rubbery microdomains spontaneously arises during polymerization in situ. The facile formation of the rubbery domains, smaller than 50 nm yet 3D continuous and cross-linked, is the key to retaining transparency above 120 °C in the visible light wavelength with dimensional stability and allowing efficient stress dissipation through the large interfacial area. We further demonstrate the 3D printability of the nanostructured materials into custom shapes via direct ink writing.

Introduction

Glassy polymers such as polystyrene (PS) and poly(-methyl methacrylate) (PMMA) are brittle and show low impact resistance. Their durability and toughness can be considerably improved by comprising rubbery polymer domains that can effectively dissipate stress[1–7]. While such domains can be produced by blending immiscible glassy and rubbery polymer pairs, the resulting impact-modified materials typically become hazy because the rubbery domains exceed several hundred nm in size and scatter visible light[8,9]. The haze issue has been challenging for optical materials such as PMMA, particularly for automobile glazing applications, where high transparency in the wide temperature range is critical to replace glass with PMMA as a lighter, mileage-friendly substitute. Commercial impact-modified PMMA contains rubbery microparticles (with a diameter of 200-300 nm) whose refractive index matches PMMA at RT by copolymerization of styrene and *n*-butyl acrylate (nBA)[10–13]. However, haze appears as temperature rises because of the change in refractive indices.

Block copolymers offer unique opportunities to transparent polymer composites, as the covalently joined polymer blocks prevent macrophase separation and effectively constrain the polymer domain size below 100 nm. Polymerization-induced microphase separation

Correspondence: Sungmin Park (parks@krict.re.kr) or Suk-kyun Ahn (skahn@pusan.ac.kr) or Myungeun Seo (seomyungeun@kaist.ac.kr)
[1]Department of Chemistry, Korea Advanced Institute of Science and Technology (KAIST), Daejeon 34141, Republic of Korea
[2]LX MMA R&D center, Daejeon 34122, Republic of Korea
Full list of author information is available at the end of the article
These authors contributed equally: Suchan Cho, Young Soo Lee, Subi Choi, Yunmi Chae

(PIMS) is an emerging block copolymer technology especially suited for facile fabrication of nanostructured thermosets[14–18]. The whole liquid polymerization mixture is converted into a monolithic product by polymerization, which drives and arrests microphase separation to produce a disordered bicontinuous morphology spontaneously. Compared to conventional block copolymer routes where synthesis and processing steps are decoupled and cross-linking should be separately performed if needed, the PIMS approach offers simultaneous cross-linking during polymerization, allowing for the rapid thermoset production with defined macroscopic shape by molding[19]. Combinations of hard and soft domains have been demonstrated to produce mechanically robust and thermally stable materials aided by cross-linking[20–27]. Notably, 3D printing has been applied to PIMS to create complex objects[28–33] as the methodology is compatible with photopolymerization[17].

Herein, we develop nanostructured PMMA block copolymer materials via the photopolymerization-based PIMS process to address challenges of conventional PMMA materials, as outlined in Scheme 1. We design the product to be composed of optically transparent and hard PMMA with impact-resistant and soft poly(*n*-butyl acrylate)(PnBA) domains. Both domains are intertwined to form a continuous network with the domain thickness ~ 50 nm without haze. We cross-link the soft domain to impart dimensional stability against temperature change. The resulting material retains high transparency and shape at 120 °C, which is around the glass transition temperature (T_g) of PMMA. In contrast, uncross-linked PMMA materials, including PMMA-*b*-PnBA-*b*-PMMA triblock copolymer, lose mechanical integrity, and commercial impact-modified PMMA develops strong haze (Scheme 1a).

To produce a covalent junction between PMMA and the PnBA network, we employ radical polymerization via the reversible addition-fragmentation chain transfer (RAFT) mechanism[34]. We prepare a homogeneous polymerization mixture consisting of PMMA macro-chain transfer agent (PMMA-CTA) dissolved in nBA and ethylene glycol diacrylate (EGDA) as a cross-linker, with 2,2-dimethoxy-2-phenylacetophenone (DMPA) as a photoradical generator. Upon irradiation with light at ambient temperature, photoinitiated copolymerization of nBA with EGDA grows the P(nBA-*co*-EGDA) network from the PMMA chain end[17,35]. Transparent and cross-linked block copolymer monoliths are rapidly produced in a scalable fashion. They retain clearness and dimensional stability even at elevated temperatures. We further demonstrate that complex transparent objects can be fabricated using direct ink writing (DIW) 3D printing to support the versatility of the PIMS-engineered PMMA materials (*Pe*PMMA) developed in this study (Scheme 1b).

Results

We produced *Pe*PMMA using PMMA-CTAs with the number-average molar mass (M_n) of 43 kg mol^{-1} in film fabrication through photo-iniferter RAFT polymerization[36] and 39 kg mol^{-1} in 3D printing through thermal polymerization to keep the viscosity of the polymerization mixture in the processable range (See the Experimental Section, Scheme S1, Fig. S1, and Table S1 for synthetic details). In a typical run, a homogeneous solution containing 30–40 wt% of PMMA-CTA and DMPA (0.6 equiv to CTA) was prepared in a mixture of nBA and EGDA. DMPA was chosen as the photoradical initiator under long UV radiation to accelerate photopolymerization following the RAFT mechanism[37,38]. The samples were designated *Pe*PMMA(*x*, *y*), where *x* and *y* represent the PMMA-CTA and the EGDA cross-linker weight fractions in the polymerization mixture, respectively.

Figure 1 demonstrates that *Pe*PMMA can be produced in various shapes, retaining high transparency and uniformity. We used a glass vial as a mold to make a monolithic cylinder (Fig. 1a). UV irradiation with a LED lamp (365 nm, 990 mW) at ambient temperature completed the polymerization within 120 min. The monomer conversion, estimated by weight loss under vacuum after polymerization, was above 90%. Significant suppression of the vinyl C=C stretching peak at 1640–1680 cm^{-1} supports high conversion and efficient network formation (Fig. S2). The surface of the monolith was also well cured due to the high initiator loading (0.6 equiv. to CTA), which provided high radical flux to suppress oxygen inhibition[39]. In the case of film fabrication, the polymerization mixture was sandwiched between two glass plates with a fixed interval (Fig. 1b and c). PMMA loading higher than 40 wt% was challenging because of the high viscosity of the solution. All the films synthesized in this study were transparent (Fig. S3). More complex shapes, such as honeycomb and octopus, were created by UV-assisted DIW 3D printing, which is discussed in detail later.

Transmission electron microscopy (TEM) of *Pe*PMMA(40, 2.5) after RuO_4 staining reveals a disordered bicontinuous morphology in *Pe*PMMA at a nanoscopic level (Fig. 1d). The light and dark domains are ascribed to glassy PMMA and rubbery P(nBA-*co*-EGDA), respectively. We estimate the interdomain distance and the PMMA domain size to be 47 ± 7 nm and 16 ± 3 nm. The observed morphology is consistent with the PIMS mechanism[16], indicating that the photoinitiated RAFT polymerization grows the P(nBA-*co*-EGDA) block from the PMMA chain end to produce the PMMA-*b*-P(nBA-*co*-EGDA) block polymer. Incompatibility between the PMMA and the growing P(nBA-*co*-EGDA) blocks intensifies as the monomer conversion and the degree of polymerization increase, resulting in spontaneous

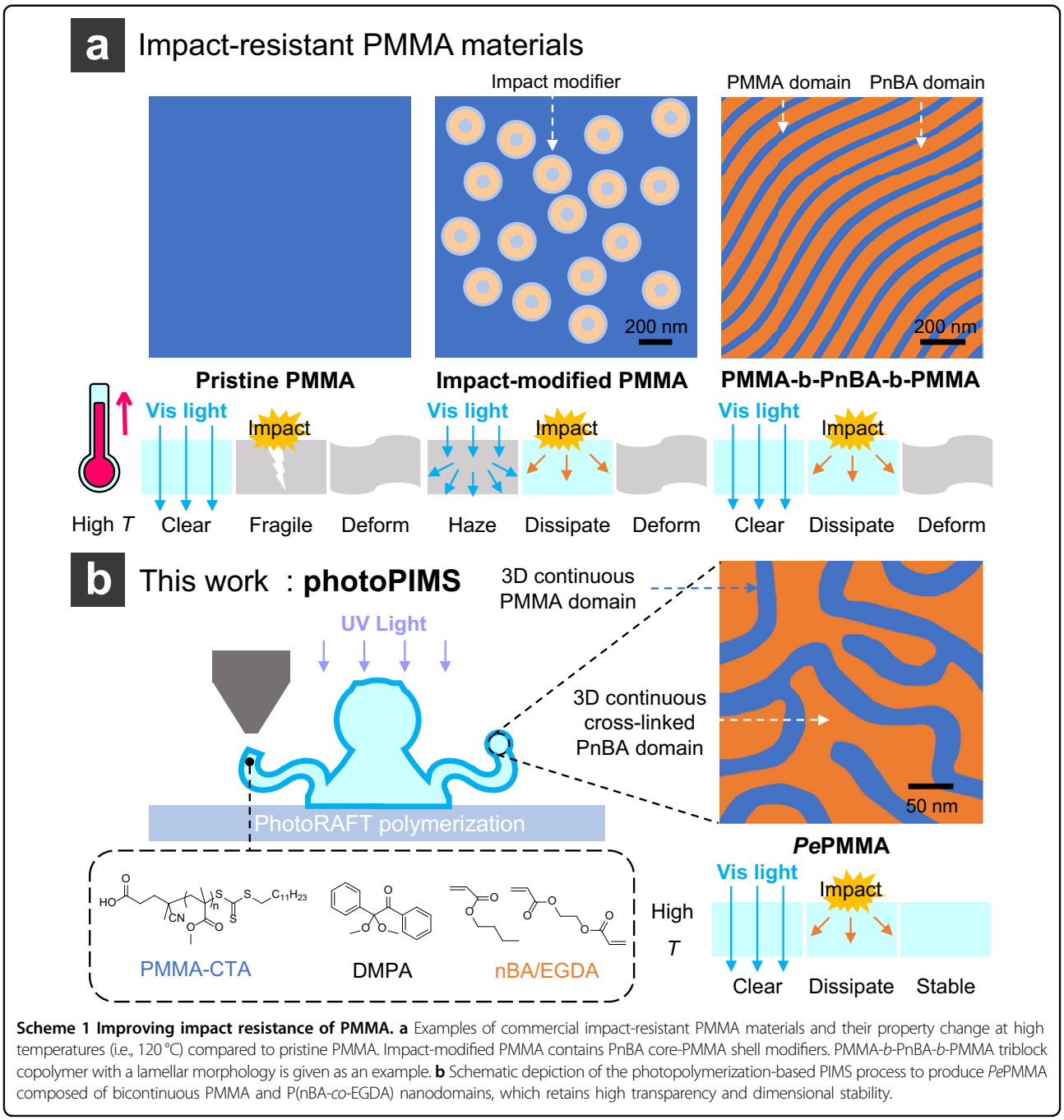

Scheme 1 Improving impact resistance of PMMA. a Examples of commercial impact-resistant PMMA materials and their property change at high temperatures (i.e., 120 °C) compared to pristine PMMA. Impact-modified PMMA contains PnBA core-PMMA shell modifiers. PMMA-*b*-PnBA-*b*-PMMA triblock copolymer with a lamellar morphology is given as an example. **b** Schematic depiction of the photopolymerization-based PIMS process to produce *Pe*PMMA composed of bicontinuous PMMA and P(nBA-*co*-EGDA) nanodomains, which retains high transparency and dimensional stability.

microphase separation. Cross-linking occurs in situ with EGDA and arrests the emergent bicontinuous morphology. The high transparency at the visible light wavelength is attributed to the microphase-separated morphology confined at the nanometer length scale, while macroscopically uniform.

We synthesized a series of samples by varying PMMA loading and the molar fraction of EGDA in the polymerization mixture to investigate their influence on the nanostructure evolution, thermal transitions, and mechanical properties. Small-angle X-ray scattering (SAXS) data of *Pe*PMMA is shown in Fig. 2a and b. A broad principal scattering peak accompanied by a second-order shoulder appears consistently throughout the samples, supporting the presence of the nanoscopic bicontinuous morphology produced by the PIMS process. For comparison, PMMA lacking the CTA moiety was synthesized via free radical polymerization (See Experimental Section, Fig. S1, and Table S1 for synthetic details) and used in the nBA/EGDA copolymerization to produce

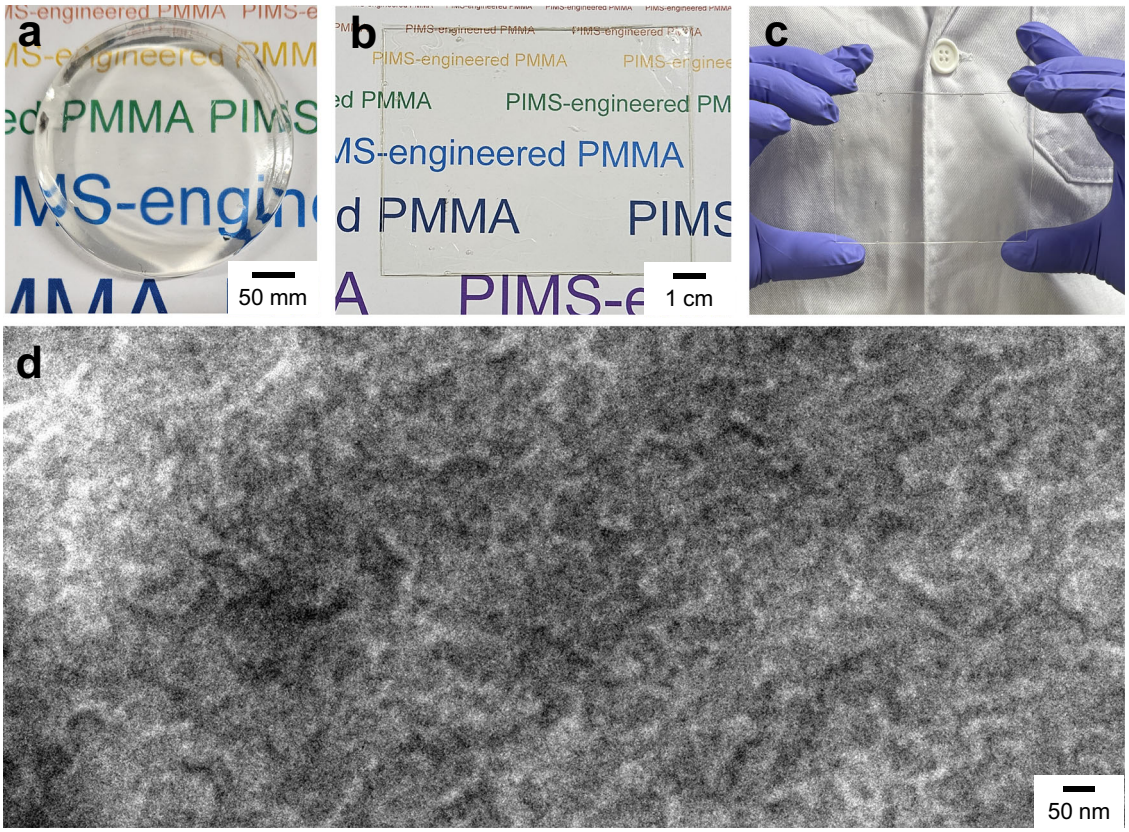

Fig. 1 *Pe*PMMA produced by photoPIMS. a–c Photos of *Pe*PMMA(40, 2.5) in different shapes. **a** Monolith (diameter = 3.7 cm, thickness = 0.7 mm). **b**, **c** Film (length × width × thickness = 9.4 cm × 7.3 cm × 1 mm). **d** Representative TEM image of *Pe*PMMA(40, 2.5) after RuO_4 staining. White and grey areas represent the PMMA and P(nBA-*co*-EGDA) domains.

an opaque and brittle monolith with cracks. No discernible scattering peak in the SAXS analysis indicates the absence of nanoscale ordering, consistent with macrophase separation occurring without the CTA[20] (Fig. S4). Decreasing the cross-linking density results in a sharper principal peak with a more pronounced shoulder, consistent with the increased local order evolved during polymerization as the structure arrest occurs later. The domain spacings (d) estimated based on the position of the principal scattering peak ($q^* = 2\pi/d$) are in the range of 46-50 nm, comparable with the TEM analysis. Using densities of PMMA (1.19 g cm^{-3}) and PnBA (1.06 g cm^{-3})[40], we estimate the PMMA volume fraction to be 0.37 at 40 wt% loading and calculate PMMA domain size of *Pe*PMMA(40, 2.5) as 18.6 nm, which is also close to the value estimated by TEM. We note that the PMMA domain size is larger than the average end-to-end distance calculated using the statistical segment length of 0.65 nm at 140 °C, indicative of PMMA chain stretching presumably due to segregation from the P(nBA-*co*-EGDA) network and the lower polymerization temperature (RT). The virtually identical nanoscopic bicontinuous morphology persists upon 30 wt% of PMMA incorporation with larger d, consistent with the previously reported literature[20].

Differential scanning calorimetry (DSC) reveals two T_gs consistent with microphase separation between the PMMA and P(nBA-*co*-EGDA) domains (Fig. 2c and d). T_g of the glassy PMMA domain appears at ~120 °C from all samples. The rubbery P(nBA-*co*-EGDA) domain exhibits T_g at a much lower temperature, which shifts to higher temperatures with the increasing cross-linking density. The glass transition becomes less pronounced above 10 wt% EGDA loading (corresponding to the molar composition of [nBA]:[EGDA] = 6.6:1), suggesting limited segmental motion of short PnBA strands between junctions.

The mechanical properties of the synthesized materials were examined by stress-strain curves at RT (Fig. 2e and Table S2). Consistent with the DSC result, an EGDA loading above 10 wt% (corresponding to the cross-linking density of 13.2%) results in brittle materials, which are characterized by a high Young's modulus (~730 MPa) and ultimate strain (~0.8%) (Table S2). This suggests that the highly cross-linked P(nBA-*co*-EGDA) network does not effectively dissipate stress. Lowering the EGDA content

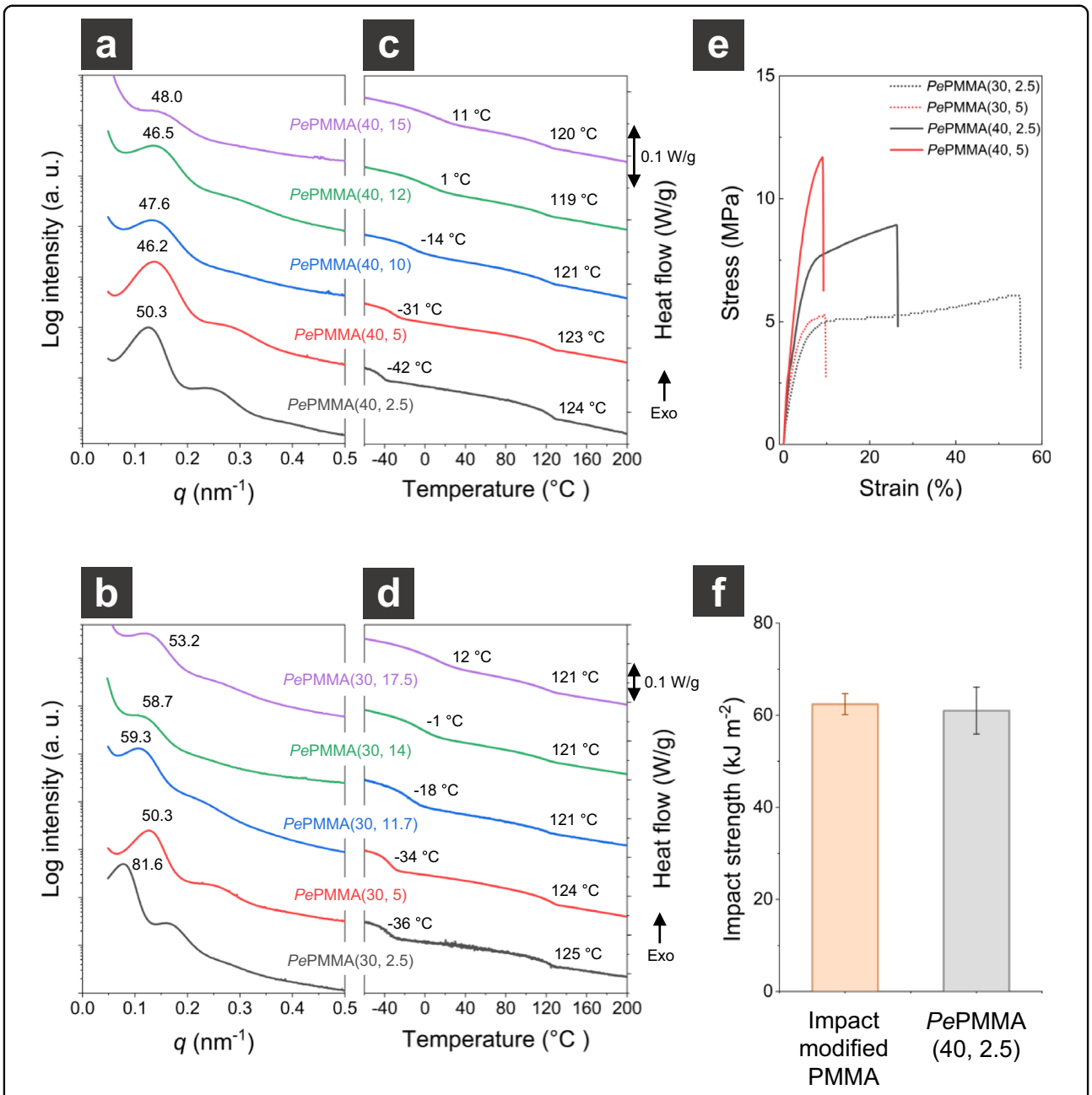

Fig. 2 Characterization of *Pe*PMMAs. a, **b** SAXS data of monolith with (a) 40 wt% and (b) 30 wt% PMMA loading including *d* (nm). DSC thermograms with (**c**) 40 wt% and (**d**) 30 wt% PMMA loading including T_gs. The data was recorded during the second heating cycle (10 °C min^{-1}, N_2) **e** Stress-strain curves at RT. **f** Impact resistance of impact-modified PMMA (orange) and *Pe*PMMA(40, 2.5) (gray).

below 10 wt% makes the material more ductile (Fig. 2e). A key factor for impact resistance is toughness, which represents the material's ability to absorb energy before failure. Reducing the EGDA weight fraction to 2.5 wt% (3.2% cross-linking) increases the toughness to ~3 MJ m^{-3}, while increasing the EGDA content to 5 wt% (6.4% cross-linking) significantly lowers the toughness. This is due to the reduced crosslinking density, which increases deformability and energy dissipation. Lowering the PMMA weight fraction (*Pe*PMMA(30, 2.5)) results in a tougher material with ~56% elongation, but reduces the Young's modulus and tensile strength compared to *Pe*PMMA(40, 2.5). The composition of *Pe*PMMA(40, 2.5) appears to offer optimal mechanical performance among the conditions we screened from the impact resistance perspective, with a well-balanced combination of energy

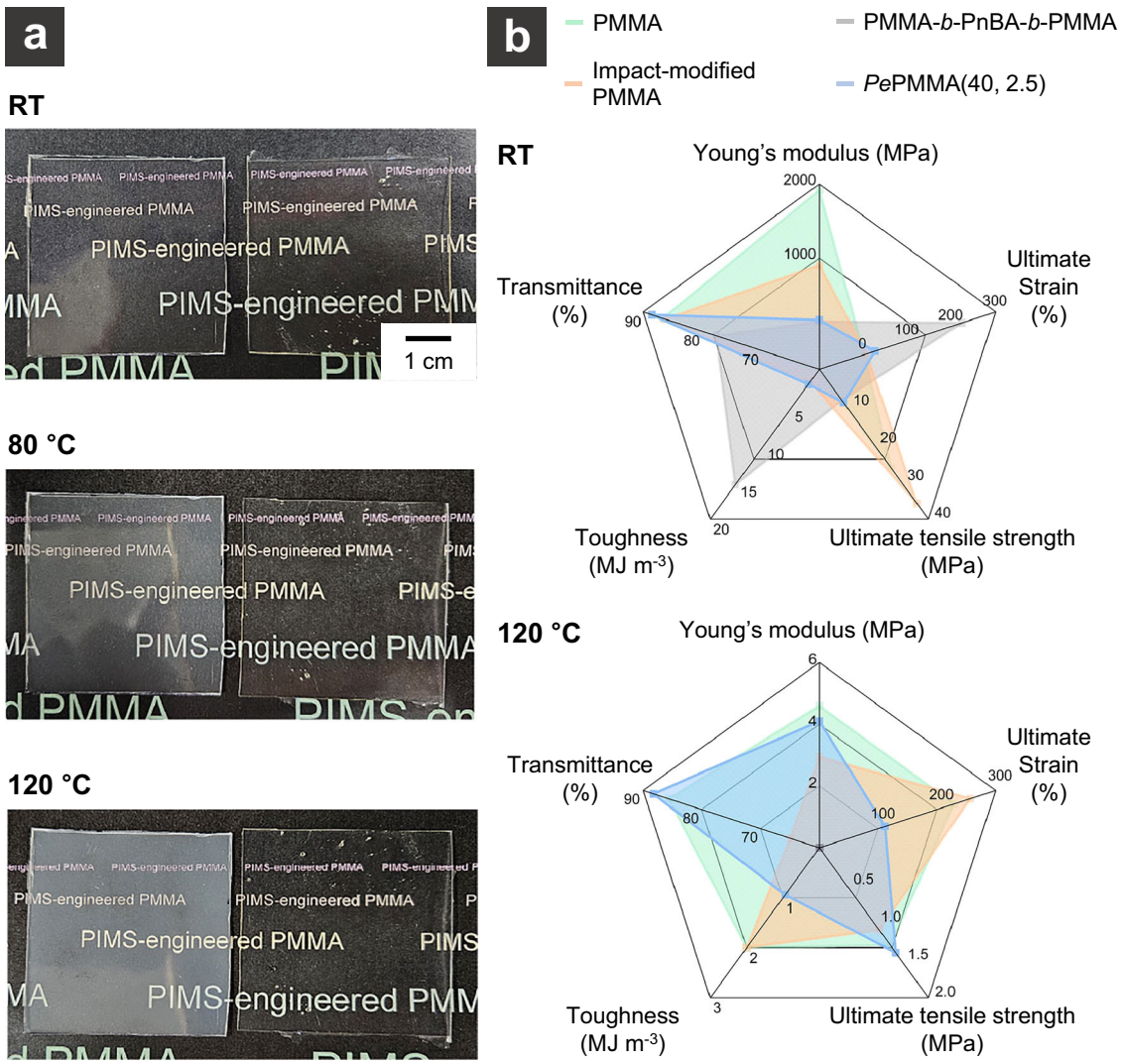

Fig. 3 Transparency and dimensional stability at high temperatures. a Photos of 1 mm-thick impact-modified PMMA (left) and *Pe*PMMA(40, 2.5) (right) at RT and after heating to 120 °C for 1 h. **b** Mechanical properties and transmittance of pristine PMMA (green), PMMA-*b*-PnBA-*b*-PMMA (gray), impact-modified PMMA (orange), and *Pe*PMMA(40, 2.5) (blue) at RT (top) and 120 °C (bottom). The *Pe*PMMA(40, 2.5) cast film shown in Fig. S3 was used for the characterization.

dissipation, deformability, and mechanical stability across all *Pe*PMMA compositions (Fig. S5). We also confirmed that *Pe*PMMA(40, 2.5) shows impact resistance similar to commercial impact-modified PMMA containing core-shell type rubbery microparticle in the unnotched Charpy impact strength test at RT (Fig. 2f and Table S3).

We evaluated the transparency and mechanical properties of *Pe*PMMA at 120 °C compared to commercially available PMMA materials. The commercial-grade pristine PMMA (known to contain a small amount of methyl acrylate repeating unit), impact-modified PMMA, and PMMA-*b*-PnBA-*b*-PMMA triblock copolymer (Nanostrength™) were chosen as references (see the Experimental Section for details). As shown in Fig. 3a, the impact-modified PMMA develops haze upon heating because of the strong scattering from the microparticles and noticeably reduces transmittance. By UV-vis spectroscopy, the transmittance drops from 86.2 to 65.0% (Fig. S6a). In contrast, the transmittance reduction of *Pe*PMMA(40, 2.5) at 120 °C compared to RT was only 0.3% from 88.5 to 88.2%, showcasing the nanostructuring effect on the material's transparency (Fig. S6b). We note that *Pe*PMMA is fairly clear in the visible light range (400–700 nm) despite a low level of the yellow trithiocarbonate moiety originating from the PMMA-CTA remains. Compared to the previously reported PIMS examples that used relatively macro CTAs with lower molar masses[41], the minimal light absorption seems to

originate from the relatively smaller number of trithiocarbonate groups incorporated in *Pe*PMMAs. To provide preliminary data on long-term optical stability, we re-evaluated the transmittance of the 6-month-old *Pe*PMMA (40, 2.5) film used in Fig. 3, Figs. S6, and S8 (Fig. S7). While the film retained its original look without any noticeable change in color by the naked eye (Fig. S7a), we noted that surface damages were present, such as micro-scratches and accumulated contaminants from repeated testing and handling (Fig. S7b). Compared to the as-synthesized film, transmittance slightly decreased from 88.5 to 82.0% at RT and 88.2 to 78.6% at 120 °C (Fig. S7c). The uncross-linked PMMA-*b*-PnBA-*b*-PMMA melted at 120 °C (Fig. S8b). The poor dimensional stability limited the triblock copolymer material from further evaluation at high temperatures. Pristine PMMA also deformed above 150 °C irreversibly (Fig. S8c).

While *Pe*PMMA(40, 2.5) does not exceed commercial PMMA materials in mechanical performance at RT, we emphasize that the main advantage of *Pe*PMMA lies in high-temperature optical and dimensional stability. *Pe*PMMA shows excellent dimensional stability up to 150 °C, retaining high transparency (Fig. S8d). We evaluated the mechanical properties of the materials at 120 °C (near the T_g of PMMA) by dynamic mechanical analysis (DMA). We summarized their performances in Fig. 3b, including optical transparency, in comparison to the metrics at RT. While all the materials show a massive drop in Young's modulus and tensile strength at 120 °C, *Pe*PMMA exhibits higher Young's moduli than impact-modified PMMA in all investigated compositions (Table S4). All the data corroborate that the 3D-continuous, cross-linked P(nBA-*co*-EGDA) domain (27–30 nm in thickness) covalently adheres to PMMA and reinforces the material against dimensional changes upon heating at the macroscopic levels (Fig. S9). We note that the PMMA-*b*-PnBA-*b*-PMMA data is missing as the specimen was fractured upon heating, signifying the importance of cross-linking (Fig. S10). Young's modulus and ultimate strain of *Pe*PMMA at 120 °C can be controlled by adjusting cross-linking density (Fig. S9). We expect room for further improving mechanical properties by using higher-molar mass PMMA and optimizing the EGDA content.

As a final demonstration, we applied DIW 3D printing to fabricate *Pe*PMMA with complex shapes. We first assessed the printability of *Pe*PMMA through rheological analysis. Liquids exhibiting shear-thinning behavior are preferred as inks because decreased viscosity under high shear rates during extrusion allows smoother flow[42]. The viscosity recovery under zero shear rate after extrusion stabilizes the printed shape. As shown in Fig. 4a, the polymerization mixtures containing 30 wt% of PMMA-CTA display relatively low viscosity with Newtonian behavior across the entire shear rate range tested (0.1 to 4000 s^{-1}). In contrast, raising PMMA loading to 40 wt% increases viscosity and exhibits the desired shear-thinning behavior at high shear rates, presumably due to chain disentanglement and molecular alignment, which reduce flow resistance. The shear stress sweep of the polymerization solutions indicated that they are viscoelastic liquids with loss moduli (G'') greater than the storage moduli (G') (Fig. 4b). While relatively high fluidity suggests that during DIW 3D printing, the material can be easily extruded through the nozzle, the dominant viscous properties imply that the printed structure should undergo rapid photocuring to maintain its shape.

Taking the *Pe*PMMA(40, 2.5) as a representative formulation, we evaluated the time-dependent evolution of dynamic moduli during UV irradiation (Fig. 4c). Immediately after UV light was turned on (at 200 s of measurement as indicated with arrow in graph), both moduli rapidly increased and G' surpasses G'', indicating sufficient solidification for the structural stability necessary for the UV-assisted DIW 3D printing. These findings confirm that *Pe*PMMA(40, 2.5) exhibits excellent flowability before UV exposure, facilitating smooth extrusion through the nozzle and rapid solidification upon UV curing, which ensures mechanical integrity and dimensional accuracy in the printed object. The honeycomb and octopus-shaped structures shown in Fig. 4e and g were successfully fabricated with excellent dimensional stability by periodically applying UV exposure for 120 s. The honeycomb-shaped *Pe*PMMA(40, 2.5) structure fabricated via DIW retained its original dimensions and geometry after thermal treatment at 120 °C for 1 h, indicating structural integrity under thermal stress (Fig. S11). SAXS analysis indicated that the 3D printed materials retain the isotropic nature of the nanoscopic morphology. We attribute the slight opaqueness of the 3D printed structures to surface light scattering caused by interlayer boundaries and surface roughness introduced during the layer-by-layer structuring in the 3D printing process[43,44]. A flower-shaped structure printed with a reduced stacking height and minimized interfacial density confirms that the material retains high optical transparency after printing (Fig. S12).

Discussion

In summary, we have successfully developed impact-resistant, haze-free PMMA materials through a photopolymerization-based PIMS process. This approach enabled the formation of transparent and mechanically robust PMMA materials with nanoscopic bicontinuous morphologies, achieved by in-situ cross-linking of rubbery PnBA domains covalently linked to glassy PMMA domains. The *Pe*PMMAs demonstrated superior

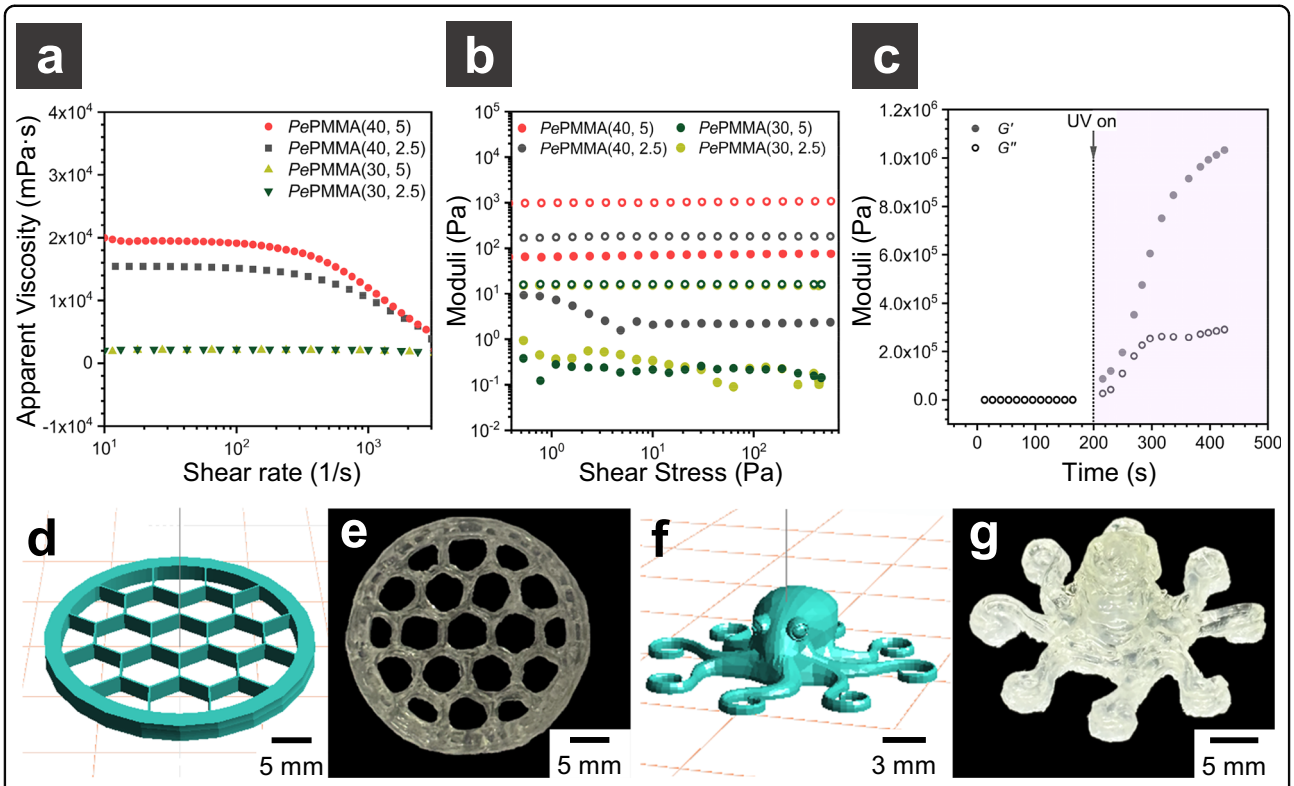

Fig. 4 DIW 3D printability of *Pe*PMMA. a Apparent viscosities as a function of shear rate for *Pe*PMMA with different compositions. **b** Storage modulus (G') and loss modulus (G'') of *Pe*PMMA (40, 2.5) as a function of shear stress. Solid circle: G'; open circle: G''. **c** Evolution of G' and G'' of *Pe*PMMA(40, 2.5) during UV curing, with UV light turned on at 180 s into the rheological run. G' and G'' cross over immediately after UV irradiation. Digital models (**d**, **f**) and 3D printed objects (**e**, **g**) of the honeycomb (**d**, **e**) and octopus (**f**, **g**) shape.

transparency, even at elevated temperatures, and exceptional impact resistance and mechanical strength. The incorporation of nanostructured, cross-linked domains significantly enhanced the thermal and dimensional stability of the material, retaining transparency and mechanical integrity at high temperature. Furthermore, the *Pe*PMMA formulations exhibited excellent processability, allowing the fabrication of complex objects via DIW 3D printing. These findings highlight the effectiveness of the PIMS process in overcoming the limitations of conventional impact-modified PMMA, such as haze and poor high-temperature performance. The ability to tailor the composition and cross-linking density further extends the versatility of *Pe*PMMA, making it a candidate for developing temperature-resistant polymer materials and provides valuable insights into potential optical applications of PIMS materials.

Experimental Section

Materials

Unless otherwise noted, all the chemicals were used as received. Methyl methacrylate (MMA) (99%), *n*-butyl acrylate (nBA) (99%), and ethylene glycol diacrylate (EGDA) (90%, technical grade) were purchased from Sigma-Aldrich (St. Louis, MO). MMA and nBA were purified by passing through a basic alumina column prior to polymerization to remove the radical inhibitor. 2,2-Dimethoxy-2-phenylacetophenone (DMPA) (≥98%) was purchased from TCI (Tokyo, Japan). Azobisisobutyronitrile (AIBN) was purchased from Junsei (Tokyo, Japan) and purified by recrystallizing from methanol. 4-Cyano-4-[(dodecylsulfanylthiocarbonyl)sulfanyl]pentanoic acid (CDTPA) was purchased from Strem Chemical (Newburyport, MA). Dimethyl sulfoxide (DMSO, 99%) was purchased from TCI and *N*,*N*-dimethylformamide (DMF, HPLC grade, 99.5%) was purchased from Daejung (Siheung, Korea). DMF was further purified with the solvent purification system (C&T International, Suwon, Korea) prior to use. Commercial pristine PMMA (IH830HF) was received from LXMMA Co. Ltd (Yeosu, Korea). Impact-modified PMMA was prepared by compounding IH830HF and a core-shell type impact modifier (PR710, 30 wt%) provided by LXMMA Co. Ltd. Commercial block copolymer PMMA-*b*-PnBA-*b*-PMMA (Nanostrength M52N) was obtained from Arkema Co. Ltd (Colombes, France). Films of PMMA materials were prepared by pressing at 240 °C and 9 kgf pressure for 20 min using a hot press.

Methods

^{1}H nuclear magnetic resonance (NMR) spectroscopy was conducted using Bruker Avance 300 and 400 MHz (Bruker, Billerica, MA) spectrometers in $CDCl_3$ with the residual NMR solvent signal as an internal reference at 7.26 ppm. Size exclusion chromatography (SEC) was performed in chloroform at 40 °C on an Agilent 1260 Infinity system (Agilent Technologies, Santa Clara, CA) with a refractive index (RI) detector and three PLgel 10 μm Mixed-B columns in series with a molar mass range 500–10,000,000 g mol^{-1}. The number average molar masses ($M_{n,SEC}$) and dispersities ($Đ$) of the polymers were calculated relative to linear PMMA standards (EasiCal) purchased from Agilent Technologies. Fourier transform infrared (FTIR) spectra were obtained on a Bruker Alpha FTIR spectrometer using a Platinum ATR (attenuation total reflection) single reflection module. Transmission electron microscopy (TEM) was performed on a Tecnai F20 (FEI company, Hillsboro, OR) field-emission transmission electron microscope with an acceleration voltage of 200 kV. Samples were prepared by cutting the 75 nm thickness epoxy resin complex with PIMS monoliths on 200 mesh carbon-coated copper grids using a PT-PC PowerTome Ultramicrotome (RMC Boeckeler, Tucson, AZ). Differential scanning calorimetry (DSC) was performed on a DSC Q25 (TA Instruments, New Castle, DE) using a scan rate of 10 °C min^{-1} under N_2 atmosphere. Synchrotron small-angle X-ray scattering (SAXS) experiments were performed at 9 A beam lines in the Pohang Accelerator Laboratory (PAL). A monochromatized X-ray radiation source of 11.09 keV with the sample-to-detector distance of 6.431 m or 19.81 keV with 6.389 m was used. Scattering intensity was monitored by a Mar 165 mm diameter CCD detector with 2048×2048 pixels. The two-dimensional scattering patterns were azimuthally integrated to afford one-dimensional profiles presented as scattering vector (q) versus scattered intensity, where the magnitude of the scattering vector is given by $q = (4\pi/\lambda)\sin(\theta/2)$. The monolith samples were analyzed without any annealing process. Stress-strain measurements were performed on a universal testing machine DR-100 (Dr TECH, Seongnam, Korea) using rectangular samples (8.0 mm (L) × 5.0 mm (W) × 0.2 mm (T)) at an elongation rate of 30 mm min^{-1} at RT. To characterize the stress-strain response at high temperatures, thermomechanical experiments were conducted using a dynamic mechanical analyzer DMA Q850 (TA instruments) equipped with a tensile clamp. For this measurement, all rectangular samples (7.0 mm × 5.0 mm × 0.2 mm) were equilibrated at 120 °C for 5 min under a preload of 0.1 N, and the force was increased at a rate of 0.5 N min^{-1}. The unnotched Charpy impact strength was measured using rectangular samples (80 mm × 10 mm × 4 mm) through a pendulum impact tester DG-UB type (Toyo Seiki Seisaku-sho, Ltd., Tokyo, Japan) according to ISO 179-2 standard and a 7.5 J hammer was used for the measurement. UV-Vis spectroscopies were conducted on a J-1500 Circular Dichroism Spectrophotometer (Jasco, Tokyo, Japan). Temperature was controlled with a Jasco PFD425S/15 Peltier-type temperature controller with a range of 25–120 °C. The spectra were recorded with PMMA films (1 mm thick) at a scanning speed of 200 nm min^{-1} and a bandwidth of 1 nm.

PMMA-CTA synthesis

We produced PMMA-CTAs used in this study via photoiniferter RAFT polymerization (for monolith and film fabrication) and thermal RAFT polymerization (for 3D printing). They are designated PMMA-CTA(x), where x represents M_n determined by SEC. In the case of photoiniferter RAFT polymerization, a polymerization mixture containing MMA (5.00 g, 50.0 mmol), CDTPA (0.0420 g, 0.104 mmol), and DMSO (12.6 mL) was prepared in a Schlenk flask equipped with a magnetic stirbar. The molar ratio was set to [MMA]:[CDTPA] = 480:1. After three cycles of freeze-pump-thaw, the flask was placed on the LED setting and polymerization was initiated by irradiation with a 1 W green LED lamp (LED MR16-1W12V-GR) ($\lambda = 515$ nm) at RT. The distance between the polymerization flask and the light source was 3 cm. The mixture was stirred for 48 h under irradiation. After turning off the LED light, the flask was opened to the air. A portion of the sample was taken from the polymerization mixture for the ^{1}H NMR (conversion). The remaining mixture was precipitated in methanol. PMMA-CTA(43) was collected by filtration of the precipitated product as a white powder and dried under vacuum at 40 °C for overnight.

For the thermal RAFT polymerization, a polymerization mixture containing MMA (20.0 g, 0.200 mol), CDTPA (0.179 g, 0.443 mmol), AIBN (7.27 mg, 0.0443 mmol), and DMF (20 mL) was prepared in a Schlenk flask equipped with a magnetic stirbar. The molar ratio was set to [MMA]:[CDTPA]:[AIBN] = 450:1:0.1. After three cycles of freeze-pump-thaw, the flask was placed in the oil bath preset at 70 °C. After stirring for 24 h, the reaction mixture was cooled to RT, and then the flask was opened to air. Following the workup procedure described above, PMMA-CTA(39) was obtained as a white powder. We also produced PMMA via free-radical polymerization. A polymerization mixture containing MMA (1.00 g, 9.99 mmol), AIBN (0.82 mg, 0.00499 mmol), and DMF (2.5 mL) was prepared in a Schlenk flask equipped with a magnetic stirbar. The molar ratio was set to [MMA]:[AIBN] = 2000:1. After three cycles of freeze-pump-thaw, the flask was placed in the oil bath preset at 70 °C. After stirring for 1 h, the reaction mixture was cooled to RT, and then the flask was opened to air.

Following the workup procedure described above, PMMA without a CTA moiety ("PMMA(FRP)") was obtained as a white powder.

Figure S1 shows a representative NMR spectrum and SEC traces of PMMA-CTAs, and their characterization details are summarized in Table S1.

Fabrication of *Pe*PMMA films

A solution of PMMA-CTA (1.00 g, 0.0232 mmol), nBA (1.44 g, 0.112 mol), EGDA (62.5 mg, 0.367 mmol), and DMPA (3.56 mg, 0.0139 mmol) were cast on a glass plate and covered with another glass plate. The weight ratio was [PMMA]:[nBA]:[EDGA] = 40:57.5:2.5. The gap between the glasses was adjusted using a spacer (0.18- or 1-mm thick). Irradiation with Aicure UJ30 (Panasonic, Osaka, Japan) through an LED head (ANUJ6186, $\lambda = 365$ nm, 990 mW) for 120 min was sufficient to produce a film with a thickness of 0.27 mm and 1 mm. The film was dried under a vacuum at 40 °C for overnight to remove the remaining monomers. The conversion was calculated with the equation:

$$Conversion(\%) = \left(1 - \frac{W_b - W_a}{W_b \times 0.6}\right) \times 100$$

W_b: weight of film before drying, W_a: weight of film after drying

For the fabrication of *Pe*PMMA(FRP) monolith, a solution of PMMA(FRP) (0.250 g, 0.00273 mmol), nBA (0.969 g, 0.756 mmol), EGDA (31.2 mg, 0.184 mmol), and DMPA (0.420 mg, 0.00164 mmol) was cast on a glass vial. The weight ratio was [PMMA]:[nBA]:[EDGA] = 20:77.5:2.5. Irradiation with Aicure UJ30 (Panasonic, Osaka, Japan) through an LED head (ANUJ6186, $\lambda = 365$ nm, 990 mW) for 120 min was sufficient to produce a monolith with a thickness of 2.3 mm.

Rheological Characterization

Rheological experiments were performed at 25 °C using a rotational rheometer MCR 101 (Anton Paar, Graz, Austria). Continuous flow tests were conducted to investigate the shear response of the material, with the shear rate linearly ramped from 0.1 to 4000 s^{-1}. Photo-rheology experiments were employed to characterize the photopolymerization kinetics of *Pe*PMMA(40, 2.5) at 25 °C using an ARES G2 rheometer (TA Instruments). Oscillatory time sweeps were carried out at an angular frequency of 1 rad s^{-1} and a strain of 1%. UV irradiation was initiated at 180 s into the time sweep experiment, with a wavelength of 365 nm and an intensity of 30 mW cm^{-2}.

UV-assisted DIW 3D Printing

Direct ink writing (DIW) 3D printing was performed using a 3D printer Dr. INVIVO 4D (Rokit Healthcare, Seoul, Korea) equipped with an extruder featuring a nozzle diameter of 0.2 mm. *Pe*PMMA(40, 2.5) ink was printed onto a build platform. The G-code for slicing CAD files of the target objects into layers was pre-programmed using NewCreatorK software. Printing was conducted at a temperature of 25 °C with a set speed of 10 mm s^{-1}. The thickness of the printed layers was controlled by adjusting the extrusion pressure, which ranged between 500 and 600 kPa. To ensure the shape stability of the printed sample, UV light (OmniCure S1500, 365 nm, 90 mW cm^{-2}) was periodically applied for 120 s at intervals throughout the printing process.

Acknowledgements

This work was supported by LX MMA and the National Research Foundation of Korea (NRF) grants funded by the Ministry of Science and ICT of Korea (2023R1A2C2005705). Experiments at Pohang Accelerator Laboratory (PAL) were supported in part by the Ministry of Science and ICT and POSTECH. We thank Jeong Beom Park and Dr. Chul Jong Han at Korea Electronics Technology Institute (KETI) for their assistance and input on photopolymerization.

Author details

[1]Department of Chemistry, Korea Advanced Institute of Science and Technology (KAIST), Daejeon 34141, Republic of Korea. [2]LX MMA R&D center, Daejeon 34122, Republic of Korea. [3]Department of Polymer Science and Engineering, Pusan National University, Busan 46241, Republic of Korea. [4]Advanced Materials Division, Korea Research Institute of Chemical Technology, Daejeon 34114, Republic of Korea. [5]KAIST Institute for Nanocentury, KAIST, Daejeon 34141, Korea

Author contributions

S.C., Y.S.L., S.C. and Y.C. contributed equally to this work. Y.S.L. and M.S. conceptualized the idea. S.C. and Y.S.L. performed polymer synthesis and characterization. S.C. evaluated the thermomechanical properties of the materials. Y.C. evaluated the rheological properties of the polymerization mixtures and performed DIW printing. S.C., Y.S.L., S.C., Y.C. and M.S. wrote the original draft. Every author reviewed and edited the manuscript. S.P., S.A. and M.S. supervised all aspects of the research.

Competing interests

The authors declare no competing interests.

Ethics approval and consent to participate

This paper is not applicable as it does not report on or involve any animals, humans, human data, human tissue, or plants.

Supplementary information The online version contains supplementary material available at https://doi.org/10.1038/s41427-025-00618-3.

Received: 6 May 2025 Revised: 3 August 2025 Accepted: 14 August 2025. Published online: 19 September 2025

References

1. Bucknall, C. B., Partridge, I. K. & Ward, M. V. Rubber toughening of plastics: Part 7 Kinetics and mechanisms of deformation in rubber-toughened PMMA. *J. Mater. Sci.* **19**, 2064–2072 (1984).
2. Bucknall, C. B. Applications of microscopy to the deformation and fracture of rubber-toughened polymers. *J. Microsc.* **201**, 221–229 (2001).

3. Lovell, P. A., McDonald, J., Saunders, D. E. J. & Young, R. J. Studies of rubber-toughened poly(methyl methacrylate): 1. Preparation and thermal properties of blends of poly (methyl methacrylate) with multiple-layer toughening particles. *Polymer* **34**, 61–69 (1993).
4. Hill, R. G. The role of microstructure on the fracture toughness and fracture behaviour of rubber-reinforced acrylics. *J. Mater. Sci.* **29**, 3062–3070 (1994).
5. Schneider, M., Pith, T. & Lambla, M. Impact modification of thermoplastics by methyl methacrylate and styrene-grafted natural rubber latexes. *Polym. Adv. Technol.* **6**, 326–334 (1995).
6. Cho, K., Yang, J. & Park, C. E. The effect of rubber particle size on toughening behaviour of rubber-modified poly(methyl methacrylate) with different test methods. *Polymer* **39**, 3073–3081 (1998).
7. Todo, M., Takahashi, K., Jar, P.-Y. B. & Béguelin, P. Toughening mechanisms of rubber toughened PMMA. *JSME Int. J. Ser. A* **42**, 585–591 (1999).
8. Conaghan, B. F. & Rosen, S. L. The optical properties of two-phase polymer systems: single scattering in monodisperse, non-absorbing systems. *Polym. Eng. Sci.* **12**, 134–139 (1972).
9. Song, J. Y., Kim, J. W. & Suh, K. D. Poly(methyl methacrylate) toughening with refractive index-controlled core–shell composite particles. *J. Appl. Polym. Sci.* **71**, 1607–1614 (1999).
10. Wrotecki, C., Heim, P. & Gaillard, P. Rubber toughening of poly(methyl methacrylate). Part I: effect of the size and hard layer composition of the rubber particles. *Polym. Eng. Sci.* **31**, 213–217 (1991).
11. Wrotecki, C., Heim, P. & Gaillard, P. Rubber toughening of poly(methyl methacrylate). Part II: effect of a twin population of particle size. *Polym. Eng. Sci.* **31**, 218–222 (1991).
12. Laatsch, J., Kim, G.-M., Michler, G. H., Arndt, T. & Süfke, T. Investigation of the micromechanical deformation behavior of transparent toughened poly(-methyl methacrylate) modified with core–shell particles. *Polym. Adv. Technol.* **9**, 716–720 (1998).
13. Ren, L., Zhang, M. Y., Han, Y., Gui, Y. & Song, L. X. Core-shell particles for design of high-performance polymeric materials with good transparency and toughness. *J. Polym. Res.* **21**, 1–7 (2014).
14. Oh, T. et al. Polymerization-induced microphase separation of a polymerization mixture into nanostructured block polymer materials. *Prog. Polym. Sci.* **145**, 101738 (2023).
15. Lee, K., Corrigan, N. & Boyer, C. Polymerization induced microphase separation for the fabrication of nanostructured materials. *Angew. Chem. Int. Ed.* **62**, e202307329 (2023).
16. Seo, M. & Hillmyer, M. A. Reticulated nanoporous polymers by controlled polymerization-induced microphase separation. *Science* **336**, 1422–1425 (2012).
17. Oh, J. & Seo, M. Photoinitiated polymerization-induced microphase separation for the preparation of nanoporous polymer films. *ACS Macro Lett.* **4**, 1244–1248 (2015).
18. Peterson, C. & Hillmyer, M. A. Fast photochromic dye response in rigid block polymer thermosets. *ACS Appl. Polym. Mater.* **1**, 2778–2786 (2019).
19. Hwang, Y. H., Oh, J., Ahn, H., Kim, D. P. & Seo, M. Synthesis of in situ microphase-separated organic–inorganic block polymer precursors to 3D-continuous mesoporous SiC-based ceramic monoliths. *ACS Appl. Polym. Mater.* **2**, 2802–2809 (2020).
20. Bobrin, V. A., Lee, K., Zhang, J., Corrigan, N. & Boyer, C. Nanostructure control in 3D printed materials. *Adv. Mater.* **34**, 2107643 (2022).
21. Bobrin, V. A. et al. Nano-to macro-scale control of 3D printed materials via polymerization induced microphase separation. *Nat. Commun.* **13**, 3577 (2022).
22. Shi, X. et al. Designing nanostructured 3D printed materials by controlling macromolecular architecture. *Angew. Chem. Int. Ed.* **61**, e202206272 (2022).
23. Xiu, Y., Bobrin, V. A., Corrigan, N., Zhang, J. & Boyer, C. Effect of macromolecular structure on phase separation regime in 3D printed materials. *Macromol. Rapid Commun.* **44**, 2300236 (2023).
24. Shi, X., Yao, Y., Zhang, J., Corrigan, N. & Boyer, C. Polymerization induced microphase separation of ABC triblock copolymers for 3D printing nanostructured materials. *Small* **20**, 2305268 (2024).
25. Xiu, Y. et al. Engineering internal nanostructure in 3D-printed materials via polymer molecular weight distribution. *J. Polym. Sci.* **62**, 766–776 (2024).
26. Wu, D., Dev, V., Bobrin, V. A., Lee, K. & Boyer, C. Nanostructure design of 3D printed materials through macromolecular architecture. *Chem. Sci.* **15**, 19345–19358 (2024).
27. Aniagbaoso, K. I. et al. In situ fabrication of quasi-solid polymer electrolytes for lithium metal battery via photopolymerization-induced microphase separation. *ACS Appl. Mater. Interfaces* **17**, 3876–3886 (2025).
28. Lee, K. et al. 3D printing nanostructured solid polymer electrolytes with high modulus and conductivity. *Adv. Mater.* **34**, 2204816 (2022).
29. Melodia, D. et al. 3D printed solid polymer electrolytes with bicontinuous nanoscopic domains for ionic liquid conduction and energy storage. *Small* **19**, 2206639 (2023).
30. Bobrin, V. A. et al. Customized nanostructured ceramics via microphase separation 3D printing. *Adv. Sci.* **10**, 2304734 (2023).
31. Bobrin, V. A. et al. Design and 3D printing of polyacrylonitrile-derived nanostructured carbon architectures. *Small Sci.* **4**, 2300275 (2024).
32. Lee, K. et al. 3D printing highly efficient ion-exchange materials via a polyelectrolyte microphase separation strategy. *Small Sci.* **4**, 2400019 (2024).
33. Bobrin, V. A. et al. Microphase separation 3D printing of binary inorganic polymer precursors to prepare nanostructured carbon-ceramic multimaterials. *Adv. Mater. Technol.* **9**, 2400337 (2024).
34. Moad, G., Rizzardo, E. & Thang, S. H. living radical polymerization by the RAFT process – a third update. *Aust. J. Chem.* **65**, 985–1076 (2012).
35. Zaquen, N. et al. Alcohol-based PISA in batch and flow: exploring the role of photoinitiators. *Polym. Chem.* **10**, 2406–2414 (2019).
36. Xu, J., Shanmugam, S., Corrigan, N. A. & Boyer, C. Catalyst-free visible light-induced RAFT photopolymerization, In *Controlled Radical Polymerization: Mechanisms*. American Chemical Society, Washington, DC, 1187, 247–267 (2015).
37. Lu, L., Yang, N. & Cai, Y. Well-controlled reversible addition-fragmentation chain transfer radical polymerisation under ultraviolet radiation at ambient temperature. *Chem. Commun* **41**, 5287–5288 (2005).
38. Lu, L., Zhang, H., Yang, N. & Cai, Y. Toward rapid and well-controlled ambient temperature RAFT polymerization under UV—Vis radiation: effect of radiation wave range. *Macromolecules* **39**, 3770–3776 (2006).
39. Lee, K., Corrigan, N. & Boyer, C. Rapid high-resolution 3D printing and surface functionalization via type I photoinitiated RAFT polymerization. *Angew. Chem. Int. Ed.* **60**, 8839–8850 (2021).
40. Penzel, E., Ballard, N. & Ausa, J. M. in *Ullmann's Encyclopedia of Industrial Chemistry*, Polyacrylate, 1-20 (Wiley-VCH, Weinheim, Germany, 2018).
41. Michelas, M., Corrigan, N. & Boyer, C. 3D printing via polymerization-induced microphase separation using acrylate macromonomers instead of macroRAFT agents. *Polym. Chem.* https://doi.org/10.1039/D5PY00226E (2025).
42. Jiang, Z. et al. Extrusion 3D printing of polymeric materials with advanced properties. *Adv. Sci.* **7**, 2001379 (2020).
43. Golhin, A. P., Tonello, R., Frisvad, J. R., Grammatikos, S. & Strandlie, A. Surface roughness of as-printed polymers: a comprehensive review. *Int. J. Adv. Manuf. Tech.* **127**, 987–1043 (2023).
44. Urrios, A. et al. 3D-printing of transparent bio-microfluidic devices in PEG-DA. *Lab Chip* **16**, 2287–2294 (2016).